Tailoring the Properties of Ammine Metal Borohydrides for Solid-State Hydrogen Storage

Lars H. Jepsen,[a] Morten B. Ley,[a] Yaroslav Filinchuk,[b] Flemming Besenbacher,[c] and Torben R. Jensen*[a]

A series of halide-free ammine manganese borohydrides, $Mn(BH_4)_2 \cdot nNH_3$, $n = 1$, 2, 3, and 6, a new bimetallic compound $Li_2Mn(BH_4)_4 \cdot 6NH_3$, and the first ammine metal borohydride solid solution $Mg_{1-x}Mn_x(BH_4)_2 \cdot 6NH_3$ are presented. Four new crystal structures have been determined by synchrotron radiation powder X-ray diffraction and the thermal decomposition is systematically investigated for all the new compounds. The solid-gas reaction between $Mn(BH_4)_2$ and NH_3 provides $Mn(BH_4)_2 \cdot 6NH_3$. The number of NH_3 per Mn has been varied by mechanochemical treatment of $Mn(BH_4)_2 \cdot 6NH_3$-$Mn(BH_4)_2$ mixtures giving rise to increased hydrogen purity for $n/m \leq 1$ for $M(BH_4)_m \cdot nNH_3$. The structures of $Mg(BH_4)_2 \cdot 3NH_3$ and $Li_2Mg(BH_4)_4 \cdot 6NH_3$ have been revisited and new structural models are presented. Finally, we demonstrate that ammonia destabilizes metal borohydrides with low electronegativity of the metal ($\chi_p < \sim 1.6$), while metal borohydrides with high electronegativity ($\chi_p > \sim 1.6$) are generally stabilized.

Introduction

Solid-state hydrogen storage materials are of high interest owing to their ability to store hydrogen in a dense way.[1–4] In metal borohydrides, hydrogen is covalently bonded to boron and this class of material has been intensively investigated during the past decade.[5–8] However, metal borohydrides tend to decompose at high temperatures due to high thermodynamic stability and sluggish kinetics. An empirical correlation between decomposition temperatures and the electronegativity of the metals in borohydrides is well established.[9–12] Thus, metal borohydrides with increasing Pauling electronegativity of the metal show decreasing decomposition temperatures, which may be below 200 °C. Unfortunately, hydrogen release is then often accompanied by formation of toxic diborane, B_2H_6.[13,14] On the contrary, formation of ammine metal borohydrides, $M(BH_4)_m \cdot nNH_3$ is a new approach, which decreases the

decomposition temperature for the stable metal borohydrides formed by metals with low electronegativity.[3,15,16] Pure hydrogen is released, presumably via the interaction between protic hydrogen, $H^{\delta+}$ in NH_3 and hydridic hydrogen, $H^{\delta-}$ from BH_4^-. Soloveichik et al. showed in 2009 for the magnesium-containing system a somewhat more complicated situation: while $Mg(BH_4)_2 \cdot 6NH_3$ releases NH_3, $Mg(BH_4)_2 \cdot 2NH_3$ releases mainly hydrogen.[15] Since then, a range of novel ammine metal borohydrides have been examined,[17–20] and one of the most successful is $Zn(BH_4)_2 \cdot 2NH_3$, which releases 8.9 wt% of pure H_2 below 115 °C within 15 min.[21] Remarkably, $Zn(BH_4)_2$ is not stable on its own and can be stabilized by less electronegative atoms in bimetallic borohydrides.[13,22] A range of other ammine metal borohydrides have been synthesized by a metathesis reaction of the ammine metal chloride, $MCl_m \cdot nNH_3$ and lithium borohydride, $LiBH_4$.[23–25] The resulting samples contain significant amounts of LiCl acting as a 'deadweight', which reduces the hydrogen storage capacity and possibly also reversibility due to formation of inert metal chlorides. Release of ammonia is detrimental for many applications, for example, in low-temperature polymer electrolyte membrane fuel cells, and needs to be reduced by proper materials design, which was recently addressed by a series of ammine magnesium borohydrides, $Mg(BH_4)_2 \cdot nNH_3$ ($n = 1$, 2, 3).[26]

The aim of this paper is to present new synthesis routes to produce different types of solvent- and halide-free ammine metal borohydrides using combined solvent-based and mechanochemical methods. We present synthesis methods, crystal structures, and new trends in thermal and gas-release properties for a new series of halide-free ammine manganese borohydrides $Mn(BH_4)_2 \cdot nNH_3$ ($n = 1$, 2, 3 and 6), a bimetallic compound $Li_2Mn(BH_4)_2 \cdot 6NH_3$, and a solid solution $Mg_{1-x}Mn_x(BH_4)_2 \cdot 6NH_3$.

[a] L. H. Jepsen, Dr. M. B. Ley, Prof. T. R. Jensen
    Center for Materials Crystallography
    Interdisciplinary Nanoscience Center (iNANO)
    and
    Department of Chemistry
    Aarhus University
    Langelandsgade 140, 8000 Aarhus C (Denmark)
    E-mail: trj@chem.au.dk

[b] Prof. Y. Filinchuk
    Institute of Condensed Matter and Nanosciences
    Université Catholique de Louvain
    Place L. Pasteur 1, 1348, Louvain-la-Neuve (Belgium)

[c] Prof. F. Besenbacher
    Interdisciplinary Nanoscience Center (iNANO)
    and
    Department of Physics and Astronomy
    Aarhus University
    Ny Munkegade 120, 8000 Aarhus C (Denmark)

Experimental Section

Sample preparation

$Mn(BH_4)_2$ was synthesized by a metathesis reaction (1), reacting $MnCl_2$ (99.999%, Sigma Aldrich) and $LiBH_4$ (95%, Sigma Aldrich) in the ratio 1:2 suspended in anhydrous diethyl ether, Et_2O, for 12 h. Et_2O was removed under vacuum at room temperature (RT) for 1 h. Subsequently, dimethyl sulfide, $S(CH_3)_2$, (dehydrated, Sigma Aldrich) was added dissolving $Mn(BH_4)_2$, followed by removal of solid LiCl by filtration. Finally, excess and coordinated $S(CH_3)_2$ was removed by using a rotary evaporator and subsequently heating the sample to 90 °C under vacuum for 3–5 h. Thereby, dry solvent- and halide-free $Mn(BH_4)_2$ was obtained. In order to avoid $LiBH_4$ in the reaction product, excess of $MnCl_2$ can be used.

$$MnCl_2 + 2\,LiBH_4 \rightarrow Mn(BH_4)_2 + 2\,LiCl \qquad (1)$$

The dense polymorph of magnesium borohydride, α-$Mg(BH_4)_2$, and the porous γ-$Mg(BH_4)_2$, were synthesized from dimethylsulfide borane $(CH_3)_2S \cdot BH_3$ and dibutylmagnesium, $Mg(nBu)_2$, through the complex $Mg(BH_4)_2 \cdot {}^1\!/_2\, S(CH_3)_2$ as described previously in the literature.[27,28]

Anhydrous $NH_3(g)$ was passed over the dry γ-$Mg(BH_4)_2$ or $Mn(BH_4)_2$ for 2–3 h at RT yielding $M(BH_4)_2 \cdot 6NH_3$ ($M = Mg$, Mn), which are denoted s1 and s2, respectively (Table 1). Remaining $LiBH_4$ in the sample leads to formation of $Li_2Mn(BH_4)_4 \cdot 6NH_3$. Alternatively, anhydrous $NH_3(g)$ was passed through the solution of $Mn(BH_4)_2$ in $S(CH_3)_2$ (denoted s3). Ammonia reacted immediately with the solution and a white precipitate formed. $S(CH_3)_2$ evaporated after 1 h, and the white precipitate was dried under vacuum at RT for another 1–2 h.

Mixtures of $Mn(BH_4)_2 \cdot 6NH_3$-$Mn(BH_4)_2$ in the molar ratios (5:1), (4:2), (3:3), (2:4) and (1:5) were mechanochemically treated using a Fritz Pulverisette 6 ball mill. These samples are denoted s4, s5, s6, s7 and s8, respectively. The powders and tungsten carbide (WC) balls (mass ratio 1:30) were loaded in a tungsten carbide vial (80 mL) under inert conditions. The powders were ball-milled at 250 rpm for 2 min intervened by a 2 min break and this sequence was repeated 60 times.

Similarly, a mixture of $Mn(BH_4)_2 \cdot 6NH_3$-$LiBH_4$ (1:2) was ball-milled at 250 rpm for 2 min followed by a 2 min pause repeated 60 times (s9). A mixture of α-$Mg(BH_4)_2$ and $Mn(BH_4)_2$ in the ratio 1:1 was ball-milled (s10), and, subsequently, the mixture was reacted with $NH_3(g)$ at RT for 2–3 h (s11).

Fractions of s7 and s8 were heated to 150 °C (4 °C min⁻¹) and kept at this temperature for 1 h in argon atmosphere and cooled to RT, denoted s7_150 and s8_150, respectively. Subsequently, the samples were characterized by PXD and FTIR. Additionally, attempts to absorb H_2 in s7_150 were performed by heating the sample to 250 °C at $p(H_2) = 145$ bar for 16 h. All handling of samples, including ammonia, and related procedures were conducted under anaerobic and anhydrous conditions by Schlenk techniques or in a glove box filled with argon.

Characterization

In-house powder X-ray diffraction (PXD): PXD measurements were performed in house in Debye–Scherrer transmission geometry using a Stoe diffractometer equipped with a curved Ge(111) monochromator ($Cu_{K\alpha1}$ radiation, $\lambda = 1.54059$ Å) and a curved position-sensitive detector. Data were collected at RT from 4° to 127° 2θ with counting times of ~960 s per step. All samples were mounted in a glove box in 0.5 mm borosilicate glass capillaries sealed with glue.

Fourier transformed infrared spectroscopy (FTIR): All samples were characterized by infrared absorption spectroscopy using a NICOLET 380 FT-IR from Thermo Electron Corporation. The samples were exposed to air for approximately 20 s prior to the data collection.

Synchrotron radiation powder X-ray diffraction (SR-PXD): In situ SR-PXD data were collected for s1 and s6 at the Swiss-Norwegian-Beamline (SNBL) at ESRF, Grenoble, France with a Pilatus area detector. The wavelength was selected to $\lambda = 0.822568$ Å (s1) and $\lambda = 0.823056$ Å (s6). The samples were packed in borosilicate glass capillaries (i.d. 0.5 mm) and heated from RT to 200 °C ($\Delta T/\Delta t = 5$ °C min⁻¹).

In situ SR-PXD data were collected for s2, s8 and s9 at I11 at Diamond, Oxford, England with a Mythen II detector and a selected wavelength of $\lambda = 0.82712$ Å (for s2) and $\lambda = 0.825654$ Å (for s8 and s9). The samples were packed in a glass capillary (i.d. 0.5 mm) and were heated from RT to 200 °C ($\Delta T/\Delta t = 5$ °C min⁻¹). Furthermore, SR-PXD patterns were obtained at RT for $Mn(BH_4)_2$, α-$Mg(BH_4)_2$, s1, s2, s10 and s11 ($\lambda = 0.825654$ Å).

Samples s2, s4 and s8 were characterized by in situ SR-PXD at the beamline I711 at the MAX-II synchrotron in the research laboratory MAX-lab, Lund, Sweden with a MAR165 CCD detector system. The samples were packed in a sapphire (Al_2O_3) single-crystal tube (1.09 mm o.d., 0.79 mm i.d.) using a specially designed sample

Table 1. Sample preparation and composition including weight fractions extracted by Rietveld refinement of SR-PXD data. The bold numbers (**1**, **2**, **3**, and **4**) denote unidentified compounds, where **3** may have the composition $Mn(BH_4)_2 \cdot NH_3$ as discussed herein. The samples s2 to s8 contain varying amounts of $LiBH_4$ producing $Li_2Mn(BH_4)_4 \cdot 6NH_3$.

Sample	Reactants	Products
s1	γ-$Mg(BH_4)_2$ + excess of NH_3	$Mg(BH_4)_2 \cdot 6NH_3$ (100 wt%)
s2	$Mn(BH_4)_2$ + excess of NH_3	$Mn(BH_4)_2 \cdot 6NH_3$ (95.4 wt%), $Li_2Mn(BH_4)_4 \cdot 6NH_3$ (4.6 wt%)
s3	$Mn(BH_4)_2(S(CH_3)_2)$ + excess of NH_3	$Mn(BH_4)_2 \cdot 6NH_3$ (~95 wt%), $Li_2Mn(BH_4)_4 \cdot 6NH_3$ (~5 wt%)
s4	$Mn(BH_4)_2 \cdot 6NH_3$-$Mn(BH_4)_2$ (5:1)[a]	$Mn(BH_4)_2 \cdot 6NH_3$ (47.0 wt%), $Mn(BH_4)_2 \cdot 3NH_3$ (31.5 wt%), $Li_2Mn(BH_4)_4 \cdot 6NH_3$ (21.5 wt%)
s5	$Mn(BH_4)_2 \cdot 6NH_3$-$Mn(BH_4)_2$ (4:2)[a]	$Mn(BH_4)_2 \cdot 3NH_3$ (50.2 wt%), $Mn(BH_4)_2 \cdot 6NH_3$ (29.9 wt%), $Li_2Mn(BH_4)_4 \cdot 6NH_3$ (18.9 wt%), $Mn(BH_4)_2 \cdot 2NH_3$ (1.1 wt%)
s6	$Mn(BH_4)_2 \cdot 6NH_3$-$Mn(BH_4)_2$ (3:3)[a]	$Mn(BH_4)_2 \cdot 3NH_3$ (75.7 wt%), $Li_2Mn(BH_4)_4 \cdot 6NH_3$ (20.7 wt%), $Mn(BH_4)_2 \cdot 6NH_3$ (2.4 wt%), $Mn(BH_4)_2 \cdot 2NH_3$ (1.3 wt%)
s7	$Mn(BH_4)_2 \cdot 6NH_3$-$Mn(BH_4)_2$ (2:4)[a]	$Mn(BH_4)_2 \cdot 2NH_3$ (~95 wt%), **1** (~5 wt%)
s8	$Mn(BH_4)_2 \cdot 6NH_3$-$Mn(BH_4)_2$ (1:5)[a]	**2** (~25 wt%), **3** (~75 wt%)
s9	$Mn(BH_4)_2 \cdot 6NH_3$-$LiBH_4$ (1:2)[a]	**4** (~90 wt%), $Li_2Mn(BH_4)_4 \cdot 6NH_3$ (~10 wt%)
s10	α-$Mg(BH_4)_2$-$Mn(BH_4)_2$ (1:1)[a]	$Mg_{1-x}Mn_x(BH_4)_2$ (38.4 wt%), $Mn(BH_4)_2$ (59.0 wt%), WC (2.6 wt%)
s11	s10 + excess of NH_3	$Mg_{0.5}Mn_{0.5}(BH_4)_2 \cdot 6NH_3$ (100 wt%)

[a] The mixture was mechanochemically treated.

holder.[29] The in situ SR-PXD measurement was performed for s2 from RT to 220 °C ($\Delta T/\Delta t = 5$ °C min^{-1}) under $p(H_2) = 100$ bar, $\lambda = 1.00989$ Å, while in situ SR-PXD data were collected for s4 and s8 from RT to 200 °C ($\Delta T/\Delta t = 5$ °C min^{-1}), $p(Ar) = 1$ bar, $\lambda = 0.99102$ Å. Finally, in situ SR-PXD data were measured for s5, s7 and s8 at the beamline P02 at Petra III, DESY, Hamburg, Germany with a Perkin-Elmer XRD 1621 detector system and wavelengths $\lambda = 0.2072$ Å for s5 and s7, and $\lambda = 0.20712$ Å for s8. The samples were mounted similarly to the samples measured at MAX-lab and in situ SR-PXD data were conducted from RT to 200 °C ($\Delta T/\Delta t = 5$ °C min^{-1}), $p(Ar) = 1$ bar.

The intensities of selected Bragg diffraction peaks were fitted to a Gaussian curve for each diffraction pattern. Subsequently, the integrated reflections were plotted in order to illustrate changes in the sample composition as a function of temperature. All obtained raw images were transformed to 2D powder diffraction patterns using the FIT2D program,[30] which was also used to remove diffraction spots from the single-crystal sapphire tube used as sample holder.

Structure solution

Mn(BH$_4$)$_2$·6NH$_3$ was indexed in a cubic unit cell, $a = 10.83410(2)$ Å using DICVOL.[31] Rietveld refinement of SR-PXD data of s2 (Supporting Information, Figure S1) confirms that Mn(BH$_4$)$_2$·6NH$_3$ is isostructural to Mg(BH$_4$)$_2$·6NH$_3$ (space group symmetry Fm-$3m$).

The Bragg peaks for Mn(BH$_4$)$_2$·3NH$_3$ were indexed in an orthorhombic unit cell with parameters $a = 11.4328(2)$, $b = 8.08692(8)$ and $c = 9.4379(1)$ Å using DICVOL. Systematic absences lead to the most likely space group $Pnma$. The peaks from the secondary compound, Li$_2$Mn(BH$_4$)$_4$·6NH$_3$, were indexed in a tetragonal unit cell with parameters, $a = 10.8177(3)$ and $c = 6.9413(3)$ Å and the space group P-$4n2$ was used in structure solution. The two structures of Mn(BH$_4$)$_2$·3NH$_3$ and Li$_2$Mn(BH$_4$)$_4$·6NH$_3$ were solved from the same SR-PXD pattern using the program FOX.[32] For the bimetallic compound, one Mn, two rigid tetrahedral BH$_4$ anions, and two rigid NH$_3$ molecules were optimized using B..B 3.3 Å, N..N 2.5 Å, and H..H 1.8 Å antibump restraints. The structure was checked for higher symmetry using ADDSYM routine in Platon,[33] which suggested higher symmetry space group $P4_2/mnm$). Indeed, atoms heavier than hydrogen follow the diagonal mirror plane symmetry. However, H-atoms around one of the two independent NH$_3$ molecules are disordered in this higher symmetry model. The fit is as good as in P-$4n2$, so the centrosymmetric but slightly disordered structural model was selected (Supporting Information, Figures S2 and S3). However, localization of hydrogen in the structure is tentative. The final Rietveld refinement for Mn(BH$_4$)$_2$·3NH$_3$ and Li$_2$Mn(BH$_4$)$_4$·6NH$_3$ against the SR-PXD data obtained for s6 is shown in Figure 1.

Mn(BH$_4$)$_2$·2NH$_3$ was indexed in an orthorhombic unit cell ($a = 17.484(2)$, $b = 9.4554(8)$, $c = 8.8731(6)$ Å). Rietveld refinement of SR-PXD data for s7 (Figure S4) confirms that Mn(BH$_4$)$_2$·2NH$_3$ is isostructural to Mg(BH$_4$)$_2$·2NH$_3$ crystallizing with space group symmetry $Pcab$.

Thermal analysis and mass spectroscopy Thermogravimetric analysis (TGA) and differential scanning calorimetry (DSC) were performed using a PerkinElmer STA 6000 apparatus simultaneously with mass spectrometry (MS) analysis of the residual gases using a Hiden Analytical HPR-20 QMS sampling system. The samples (approx. 5 mg) were placed in an Al$_2$O$_3$ crucible and heated from 40 to 400 °C (5 °C min^{-1}) in an argon flow of 20 mL min^{-1}. The released gas was analyzed for hydrogen, ammonia, diborane, and dimethyl sulfide.
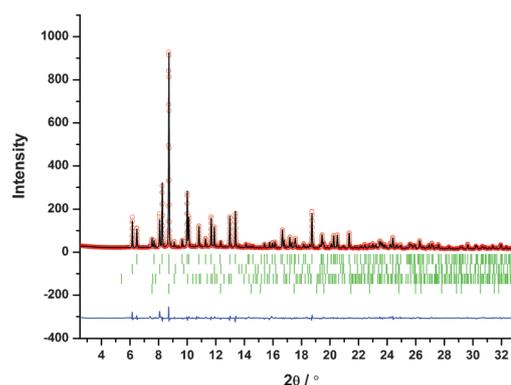
Figure 1. Rietveld refinement of SR-PXD data for Mn(BH$_4$)$_2$·6NH$_3$-Mn(BH$_4$)$_2$ (3:3, s6) measured at RT, $\lambda = 0.823065$ Å. "Tic marks" Mn(BH$_4$)$_2$·3NH$_3$ (top), Li$_2$Mn(BH$_4$)$_4$·6NH$_3$, Mn(BH$_4$)$_2$·2NH$_3$ and Mn(BH$_4$)$_2$·6NH$_3$.

Temperature-programmed photographic analysis Approx. 10 mg of s2, s6, s7, s8 and s9 were sealed under argon in a glass tube and placed in a home-built aluminum heating block as described recently.[34] The samples were heated from RT to 300 °C ($\Delta T/\Delta t = 4$ °C min^{-1}), while photos of the samples were collected every five seconds.

Results and Discussion

Initial sample characterization

Powder X-ray diffraction (PXD) data of s1 reveal that a reaction between γ-Mg(BH$_4$)$_2$ and dry NH$_3$ at RT yields the known cubic Mg(BH$_4$)$_2$·6NH$_3$ ($a = 10.7948(2)$ Å) compound (Supporting Information, Figure S5). The structure of Mg(BH$_4$)$_2$·6NH$_3$ was solved recently and is isostructural to MgCl$_2$·6NH$_3$.[15] Thus, ammonia molecules coordinate to magnesium to form [Mg(NH$_3$)$_6$]$^{2+}$ complexes rather than physisorp to the porous framework structure of γ-Mg(BH$_4$)$_2$. Similar PXD patterns (Figure S5) were obtained for dry Mn(BH$_4$)$_2$ and for Mn(BH$_4$)$_2$ in S(CH$_3$)$_2$ reacted with NH$_3$ (s2 or s3) revealing formation of a new ammine manganese borohydride, Mn(BH$_4$)$_2$·6NH$_3$, isostructural to Mg(BH$_4$)$_2$·6NH$_3$.

Mixtures of Mn(BH$_4$)$_2$·6NH$_3$-Mn(BH$_4$)$_2$ (5:1, s4), (4:2, s5), (3:3, s6), (2:4, s7) and (1:5, s8) have been mechanochemically treated and the products characterized by PXD and compared in Figure 2. The weight fractions of the reaction products extracted by Rietveld refinement are listed in Table 1. PXD data for s2 (Figure 2) show Bragg reflections from Mn(BH$_4$)$_2$·6NH$_3$ and weak peaks from Li$_2$Mn(BH$_4$)$_4$·6NH$_3$. The formation of Li$_2$Mn(BH$_4$)$_4$·6NH$_3$ is likely caused by a minor solubility of LiBH$_4$ in S(CH$_3$)$_2$ or via formation of the coordination framework compound [(Li(Et$_2$O)$_2$)(Mn$_2$(BH$_4$)$_5$)] during the synthesis procedures.[35] PXD data for s4 and s5 show that the samples contain a mixture of Mn(BH$_4$)$_2$·6NH$_3$, Mn(BH$_4$)$_2$·3NH$_3$, and Li$_2$Mn(BH$_4$)$_4$·6NH$_3$, indicating that Mn(BH$_4$)$_2$·nNH$_3$ ($n = 4$, 5) are not formed under the used conditions. PXD data for s6 contain reflections from Mn(BH$_4$)$_2$·3NH$_3$, Li$_2$Mn(BH$_4$)$_4$·6NH$_3$, Mn(BH$_4$)$_2$·2NH$_3$ and Mn(BH$_4$)$_2$·6NH$_3$, while PXD data for s7 reveal the presence of Mn(BH$_4$)$_2$·2NH$_3$ and a few weak unidentified re-
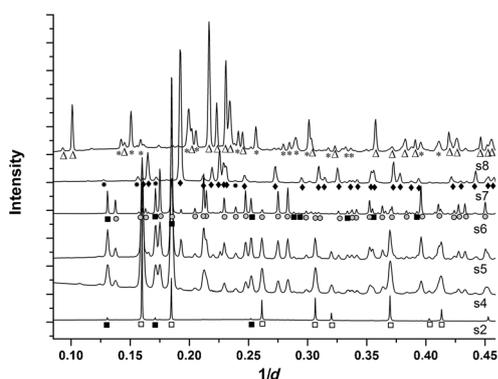
Figure 2. PXD patterns of $Mn(BH_4)_2 \cdot 6NH_3$ (s2), $Mn(BH_4)_2 \cdot 6NH_3$-$Mn(BH_4)_2$ (5:1, s4), (4:2, s5), (3:3, s6), (2:4, s7) and (1:5, s8). Symbols: □ $Mn(BH_4)_2 \cdot 6NH_3$; ● $Mn(BH_4)_2 \cdot 3NH_3$; ■ $Li_2Mn(BH_4)_4 \cdot 6NH_3$; ◆ $Mn(BH_4)_2 \cdot 2NH_3$; ● **1**; * **2**; △ **3**.

Figure 3. The crystal structure of $Mn(BH_4)_2 \cdot 6NH_3$. Mn^{2+} (orange) is octahedrally coordinated by six N-atoms (N green) in NH_3 molecules forming the complex $[Mn(NH_3)_6]^{2+}$, while BH_4^- (blue tetrahedron) acts as counter ions in the crystalline solid. Hydrogen atoms in BH_4^- are light gray, while hydrogen atoms in NH_3 are now shown for simplicity.

flections denoted **1** ($d = 7.85$, 6.40, 5.82, 5.53, 4.19, 3.32, 2.98, and 2.58 Å). PXD data for s8 contain reflections from two new compounds, denoted **2** (minor amount) and **3** (major). Compound **2** is indexed in an orthorhombic unit cell $a = 13.2970(6)$, $b = 8.2900(4)$, $c = 7.1740(4)$ Å ($V = 790.80(5)$ Å^3) and consists likely of a bimetallic borohydride ammoniate with low NH_3 content, as for example $Li_2Mn(BH_4)_4 \cdot NH_3$, while compound **3** ($d = 10.755$, 9.981, 8.525, 6.873, 5.364, 4.950, 4.613, 4.447, 4.325, 4.268, 4.073, 3.298, and 3.095 Å) may have the composition $Mn(BH_4)_2 \cdot NH_3$. However, attempts to index **3** have been unsuccessful.

In order to obtain a pure sample of $Li_2Mn(BH_4)_4 \cdot 6NH_3$, a mixture of $Mn(BH_4)_4 \cdot 6NH_3$-$LiBH_4$ (1:2, s9) was prepared. Surprisingly, SR-PXD data for s9 (Supporting Information, Figure S6) show reflections from two compounds, mainly from an unidentified compound denoted **4** and minor reflections from $Li_2Mn(BH_4)_4 \cdot 6NH_3$. Attempts to index **4** ($d = 7.550$, 7.446, 6.711, 5.664, 5.296, 5.018, 4.979, 4.161, 3.887, 3.857, and 3.774 Å) were unsuccessful.

Structural chemistry

A total of four new compounds with high hydrogen contents and different structures are listed in Table 2, and the atomic co-
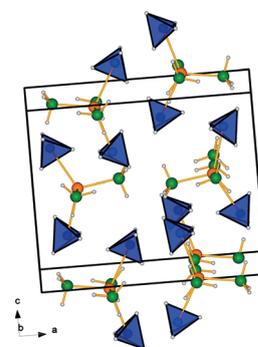
ordinates are provided in Tables S1, S2, S3, and S4 (Supporting Information). The crystal structure of $Mn(BH_4)_2 \cdot 6NH_3$ is presented in Figure 3. Mn is octahedrally coordinated by six NH_3 groups with a Mn–N bond distance of 2.267(1) Å (2.2398 Å in $Mn(NH_3)_6Cl_2$[36] forming $[Mn(NH_3)_6]^{2+}$ complexes, while BH_4 acts as counter ions in the crystalline solid. The unit cell axis for $Mn(BH_4)_2 \cdot 6NH_3$ ($a = 10.83410(2)$ Å) is only 0.0393 Å larger than for $Mg(BH_4)_2 \cdot 6NH_3$ ($a = 10.7948(2)$ Å), corresponding to a difference in unit cell volumes of only 1.08 % even though there is a larger difference in ionic radii of Mn^{2+} (0.80 Å) compared to Mg^{2+} (0.71 Å) of 11.25 %.[37]

In the structure of $Mn(BH_4)_2 \cdot 3NH_3$, Mn coordinates to two BH_4 anions and three NH_3 molecules, two of the latter are in the apical positions (N-Mn-N angle 172.52(9)°), see Figure 4. The N-
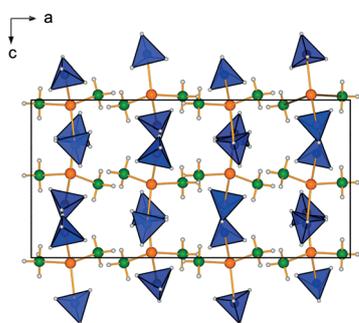

Figure 4. The crystal structure of $Mn(BH_4)_2 \cdot 3NH_3$. Manganese ions, Mn^{2+} (orange), coordinates to three NH_3 (N green) groups and two BH_4^- (blue tetrahedron) forming neutral molecular complexes in the solid state, $[Mn(NH_3)_3(BH_4)_2]$. Hydrogen atoms are light gray.

Mn-B angles are between 86.7(1) and 110.9(2)°, and the other N-Mn-N angle is 92.99(9)°. The Mn-B distances are 2.518(5) and 2.497(6) Å, respectively, while the three Mn-N distances are 2.163(6), 2.205(2) and 2.205(2) Å, respectively. This coordination is similar to the coordination for Mg in $LiMg(BH_4)_3 \cdot 2NH_3$.[38] NH_3 and BH_4 groups act as terminal ligands making the structure consist of neutral molecules $[Mn(BH_4)_2(NH_3)_3]$. The mononuclear molecular structure of $Mn(BH_4)_2(NH_3)_3$ is not typical for metal borohydrides, but it also

Table 2. Structural data and hydrogen content for the new ammine manganese borohydrides.

Chemical formula	$Mn(BH_4)_2 \cdot 6NH_3$	$Mn(BH_4)_2 \cdot 3NH_3$	$Mn(BH_4)_2 \cdot 2NH_3$	$Li_2Mn(BH_4)_4 \cdot 6NH_3$
Crystal system	cubic	orthorhombic	orthorhombic	tetragonal
Space group	$Fm\text{-}3m$	$Pnma$	$Pcab$	$P4_2/mnm$
a [Å]	10.83410(2)	11.4328(2)	17.484(2)	10.8177(3)
b [Å]	–	8.08692(8)	9.4554(8)	–
c [Å]	–	9.4379(1)	8.8731(6)	6.9413(3)
V [Å^3]	1271.68(0)	872.59(2)	1466.9(2)	812.29(4)
Z	4	4	8	2
M [g mol^{-1}]	186.81	135.72	118.68	230.37
ρ (calc.) [g mL^{-1}]	0.9757	1.033	1.075	0.9419
$\rho_m(H_2)$ [wt %]	14.0	12.6	11.9	14.9
$\rho_v(H_2)$ [kg H$_2$ m^{-3}]	136.9	130.4	127.8	140.1

occurs for $Zr(BH_4)_4$, $Al(BH_4)_3$ and $Mg(BH_4)_2(NH_3BH_3)_2$.[28,39–41] The shortest H..H distance between H from to different ligands is between $H^{\delta+}$ on NH_3 (H18) and $H^{\delta\circ}$ on BH_4 (H8) that are separated by 2.189(5) Å (considering non-corrected H-positions obtained from X-ray data).[42] Recently, the magnesium analogue, $Mg(BH_4)_2 \cdot 3NH_3$, was indexed in an orthorhombic unit cell ($a =$ 7.432, $b = 6.149$, $c = 23.124$ Å) significantly different from the unit cell of $Mn(BH_4)_2 \cdot 3NH_3$, while the crystal structure was not solved.[26] In fact, $Mg(BH_4)_2 \cdot 3NH_3$ is isostructural to $Mn(BH_4)_2 \cdot 3NH_3$ presented in this study (Supporting Information, Figure S7).

$Mn(BH_4)_2 \cdot 2NH_3$ crystallizes in an orthorhombic unit cell, $a =$ 17.484(2), $b = 9.4554(8)$, $c = 8.8731(6)$ Å, with space group symmetry $Pcab$ and is isostructural to $Mg(BH_4)_2 \cdot 2NH_3$, $a =$ 17.4872(4), $b = 9.4132(2)$, $c = 8.87304(2)$ Å.[15] The two compounds have almost identical unit cell volumes, which differ by only 0.43%. Mn^{2+} coordinates to two NH_3 molecules and two BH_4^- groups forming neutral molecular complexes of $[Mn(NH_3)_2(BH_4)_2]$, see Figure 5. The bond lengths Mn-B are

Figure 5. The crystal structure of $Mn(BH_4)_2 \cdot 2NH_3$. Mn^{2+} (orange) is coordinated by two NH_3 molecules (N green) and two BH_4^- complexes (blue tetrahedron), forming neutral molecular complexes, $[Mn(NH_3)_2(BH_4)_2]$. Hydrogen atoms are light gray.

2.33(7) and 2.49(7) Å, while the distances Mn-N are 2.21(5) and 2.38(8) Å. The angle N-Mn-N is slightly smaller (104.8(2)°) compared to the B-Mn-B angle (116.2(8)°).

The tetragonal structure of $Li_2Mn(BH_4)_4 \cdot 6NH_3$ (space group symmetry $P4_2/mnm$) is shown in Figure 6. Manganese is octahedrally coordinated by six NH_3 forming $[Mn(NH_3)_6]^{2+}$ complexes, while Li coordinates to four BH_4. Thereby, the structure is built of distinct $[Mn(NH_3)_6]^{2+}$ complex ions counter-balanced by one-dimensional $[Li_2(BH_4)_4]_n^{2-}$ polymers. Mn–N bond lengths (2.51(5) to 2.67(4) Å) are slightly longer than in $Mn(BH_4)_2 \cdot 6NH_3$ (2.267(1) Å). The N–Mn–N bond angles vary in the range 87.159(1) to 92.841(1)°. Li is coordinated by edge-sharing (η^2) BH_4, where each BH_4 group coordinates two Li atoms forming a $[Li_2(BH_4)_4]_n^{2-}$ polymer chain along the [001] direction. The Li–B bond lengths (2.534 to 2.696 Å) are slightly longer than in $LiBH_4$ (2.3736 Å).[43] To date, five bimetallic borohydride ammoniates are reported, that is, $Li_2Al(BH_4)_5 \cdot 6NH_3$,[17] $LiMg(BH_4)_3 \cdot 2NH_3$,[38] $LiSc(BH_4)_4 \cdot 4NH_3$,[24] $NaZn(BH_4)_3 \cdot 2NH_3$[44] and $Li_2Mg(BH_4)_4 \cdot 6NH_3$.[45] Similar to $Li_2Mn(BH_4)_4 \cdot 6NH_3$, $Li_2Al(BH_4)_5 \cdot 6NH_3$ consists of ordered metal ammine complexes, $[Al(NH_3)_6]^{3+}$, and complex anions, $[Li_2(BH_4)_5]^{3-}$. Recently,
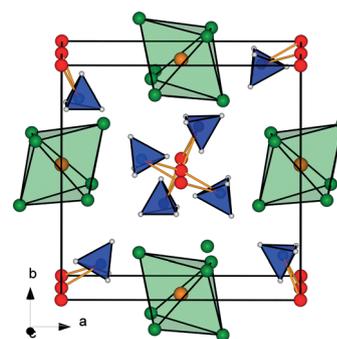
Figure 6. The crystal structures of $Li_2Mn(BH_4)_4 \cdot 6NH_3$. Manganese, Mn^{2+} (orange), is octahedrally coordinated by six nitrogen atoms (N green) in NH_3 molecules forming $[Mn(NH_3)_6]^{2+}$ complexes. Lithium, Li^+ (red), is coordinated by four BH_4^- complexes (blue tetrahedra) forming a $[Li_2(BH_4)_4]_n^{2-}$ polymer along the [001] direction. Hydrogen atoms are light gray in BH_4^-, while hydrogen atoms in NH_3 are now shown for simplicity.

$Li_2Mg(BH_4)_4 \cdot 6NH_3$ was reported to crystallize in a tetragonal unit cell with twice longer c-axis ($a = 10.7656(8)$ and $c =$ 13.843(1) Å and space group symmetry $P4_32_12$)[45] as compared to the structural model for $Li_2Mn(BH_4)_4 \cdot 6NH_3$ presented here. We have carefully examined the structural model for $Li_2Mg(BH_4)_4 \cdot 6NH_3$ using the ADDSYM routine in Platon,[33] which in fact suggests a smaller unit cell by reduction of the length of the c-axis and suggests the higher space group symmetry $P4_2/mnm$. Indeed, the structural model for $Li_2Mg(BH_4)_4 \cdot 6NH_3$ has a pseudo-translation along z reducing the c-axis length by a factor of two. Furthermore, no superstructure peaks are observed for either $Li_2Mg(BH_4)_4 \cdot 6NH_3$ or $Li_2Mn(BH_4)_4 \cdot 6NH_3$. Thus, we demonstrate that $Li_2Mg(BH_4)_4 \cdot 6NH_3$ and $Li_2Mn(BH_4)_4 \cdot 6NH_3$ are isostructural and the correct structural model is presented in this work for $Li_2Mn(BH_4)_4 \cdot 6NH_3$.

The unit cell volumes per formula unit (V/Z) at RT as a function of the number of ammonia molecules in the formula unit n for $Mn(BH_4)_2 \cdot nNH_3$ ($n = 0, 2, 3, 6$) and $Li_2Mn(BH_4)_4 \cdot 6NH_3$ reveal a linear relationship (Figure 7). The slope of the straight line is 34.0 Å^3 ($R^2 = 0.9998$) reflecting the size of one ammonia mole-
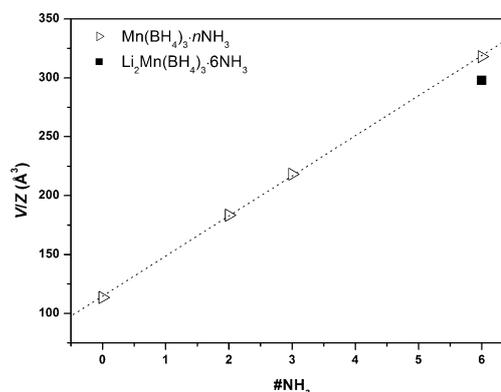

Figure 7. Unit cell volumes (V) at RT divided by the number of formula units (Z) plotted as a function of the number of ammonia molecules in the formula unit, $Mn(BH_4)_2 \cdot nNH_3$ ($n = 0, 2, 3, 6$). The unit cell volume of $Li_2Mn(BH_4)_4 \cdot 6NH_3$ subtracted the volume of two formula units of $LiBH_4$ (data from Ref. [47]) is shown as a black square.

cule, which in solid NH_3 at $-80\,°C$ is $V(NH_3) = 33.9\,Å^3$.[46] The volume of two $LiBH_4$ ($V(LiBH_4) = 54.2\,Å^3$)[47] has been subtracted for $Li_2Mn(BH_4)_4\cdot6NH_3$, which has a slightly lower V/Z than $Mn(BH_4)_2\cdot6NH_3$.

Fourier transformed infrared spectroscopy

The porous polymorph γ-$Mg(BH_4)_2$, $Mn(BH_4)_2$ and $Mn(BH_4)_2$ in $S(CH_3)_2$ all react with NH_3 (s1, s2 and s3), and produce $M(BH_4)_2\cdot6NH_3$ ($M = Mg$, Mn). FTIR spectra recorded for the three samples (Supporting Information, Figure S8) are similar for the isostructural compounds, $Mg(BH_4)_2\cdot6NH_3$ and $Mn(BH_4)_2\cdot6NH_3$. Furthermore, no absorption bands from C—H or S—C are observed, reflecting that all $S(CH_3)_2$ has been removed.

FTIR has been measured for $Mn(BH_4)_2\cdot6NH_3$-$Mn(BH_4)_2$ (5:1, s4), (4:2, s5), (3:3, s6), (2:4, s7) and (1:5, s8) (Figure 8 and Sup-
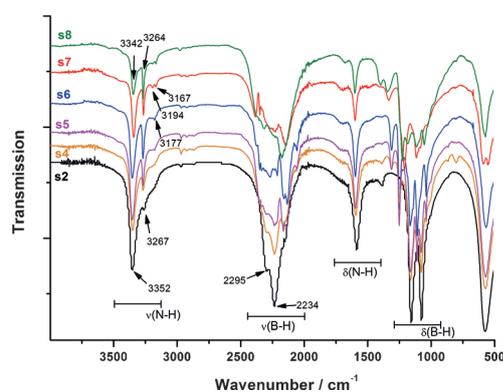
Figure 8. Fourier transform infrared spectroscopy data for $Mn(BH_4)_2\cdot6NH_3$ (s2), $Mn(BH_4)_2\cdot6NH_3$-$Mn(BH_4)_2$ (5:1, s4), (4:2, s5), (3:3, s6), (2:4, s7) and (1:5, s8).

porting Information, Table S5). All samples reveal at least two clear signals in the N—H stretch region, that is, from 3400 to 3100 cm^{-1}. For s2, s4, s5 and s6 that contain $Mn(BH_4)_2\cdot6NH_3$, $Mn(BH_4)_2\cdot3NH_3$ and $Li_2Mn(BH_4)_4\cdot6NH_3$ the maxima are at ~3352 and ~3267 cm^{-1}, while the maxima for s7 and s8 which contain $Mn(BH_4)_2\cdot2NH_3$, **1**, **2**, and **3** are at a slightly lower wavenumber, that is, 3342 and 3264 cm^{-1}. FTIR spectra for s4, s5 and s6 that all contain $Mn(BH_4)_2\cdot3NH_3$ have an additional signal at 3177 cm^{-1}, while two extra signals at 3167 and 3194 cm^{-1} are observed for s7 ($Mn(BH_4)_2\cdot2NH_3$ and **1**) and s8 (**2** and **3**). For $Mn(BH_4)_2\cdot6NH_3$ (s2), the NH_3 molecules are all bonded to the metal in ordered octahedron giving rise to only two visible vibration modes. In contrast, for $Mn(BH_4)_2\cdot2NH_3$ (s7) the NH_3 coordination to the metal is less ordered giving rise to more N-H vibrations. A similar behavior is therefore expected for the crystal structure of $Mn(BH_4)_2\cdot NH_3$ (s8). The B-H region is similarly more complex for the compounds with lower content of ammonia. For $Mn(BH_4)_2\cdot6NH_3$ (s2) all BH_4^- groups act as counter ions and do not bond directly to the metal giving maximum frequencies at 2234 and 2295 cm^{-1} similar to values observed for a range of metal borohydrides.[48] For samples s4–s8 more

bands appear with maximum intensities shifted to slightly lower frequencies (Supporting Information, Table S5), that is, in the range from 2174 to 2130 cm^{-1}.

In situ SR-PXD investigation

In situ SR-PXD data have been collected for $Mg(BH_4)_2\cdot6NH_3$ (s1), $Mn(BH_4)_2\cdot6NH_3$ (s2), $Mn(BH_4)_2\cdot6NH_3$-$Mn(BH_4)_2$ (5:1, s4), (4:2, s5), (3:3, s6), (2:4, s7), (1:5, s8) and $Mn(BH_4)_2\cdot6NH_3$-$LiBH_4$ (1:2, s9) from RT to ~200 $°C$, $\Delta T/\Delta t = 5\,°C\,min^{-1}$ in argon atmosphere. Detailed description of in situ SR-PXD experiments for s4, s5, and s6 can be found in the Supporting Information. Table 3

Table 3. Overview of the samples investigated by in situ SR-PXD heated in argon atmosphere with $5\,°C\,min^{-1}$. The compounds formed during the synthesis procedure are reported, while T_{form} denotes the formation temperature during heating. T_{max} denotes the maximum temperature where the crystalline compounds are observed.

Sample	Compounds	T_{form} [$°C$]	T_{max} [$°C$]
s1	$Mg(BH_4)_2\cdot6NH_3$ (100 wt%)		~188
s2	$Mn(BH_4)_2\cdot6NH_3$ (95.4 wt%)		~160
	$Li_2Mn(BH_4)_4\cdot6NH_3$ (4.6 wt%)		~95
s4	$Mn(BH_4)_2\cdot3NH_3$ (31.5 wt%)		~59
	$Li_2Mn(BH_4)_4\cdot6NH_3$ (21.5 wt%)		~68
	$Mn(BH_4)_2\cdot6NH_3$ (47.0 wt%)	~65	
	$Mn(BH_4)_2\cdot6NH_3$ (100 wt%)		~116
s5	$Mn(BH_4)_2\cdot2NH_3$ (1.1 wt%)		~59
	$Mn(BH_4)_2\cdot3NH_3$ (50.2 wt%)		~62
	$Li_2Mn(BH_4)_4\cdot6NH_3$ (18.9 wt%)		~67
	$Mn(BH_4)_2\cdot6NH_3$ (29.9 wt%)	~63	
	$Mn(BH_4)_2\cdot6NH_3$ (100 wt%)		~126
s6	$Mn(BH_4)_2\cdot2NH_3$ (1.3 wt%)		~57
	$Mn(BH_4)_2\cdot3NH_3$ (75.7 wt%)		~65
	$Li_2Mn(BH_4)_4\cdot6NH_3$ (20.7 wt%)		~65
	$Mn(BH_4)_2\cdot6NH_3$ (2.4 wt%)	~63	
	$Mn(BH_4)_2\cdot6NH_3$ (100 wt%)		~110
s7	**1** (~5 wt%)		~45
	$Mn(BH_4)_2\cdot2NH_3$ (95 wt%)		~77
s8	**2** (~25 wt%)		~52
	3 (~75 wt%)		~41
s9	**4** (~90 wt%)		~80
	$Li_2Mn(BH_4)_4\cdot6NH_3$ (~10 wt%)		~100

shows an overview of the results obtained from the in situ SR-PXD measurements for all the samples.

In situ SR-PXD data measured for $Mg(BH_4)_2\cdot6NH_3$ (s1) are shown in Figure S9 (Supporting Information). The integrated intensities of selected Bragg peaks from each pattern are plotted in Figure S10 A (Supporting Information). At RT all Bragg peaks can be assigned to $Mg(BH_4)_2\cdot6NH_3$ and the diffracted intensity decreases slowly from $T \approx 40\,°C$ and disappears at 188 $°C$. An X-ray amorphous product was obtained after this experiment (heating to 200 $°C$). In situ SR-PXD has been measured for $Mn(BH_4)_2\cdot6NH_3$ and $Li_2Mn(BH_4)_4\cdot6NH_3$ (s2) heated from RT to 200 $°C$ ($\Delta T/\Delta t = 5\,°C\,min^{-1}$) in argon atmosphere (Supporting Information, Figure S11 and Figure S10 B). The weak reflections from $Li_2Mn(BH_4)_4\cdot6NH_3$ decrease in intensity from $T \approx 65$ and disappear at 95 $°C$ without any new reflections appearing. $Mn(BH_4)_2\cdot6NH_3$ shows similar low thermal stability and

the diffraction peaks decrease in intensity and disappear in the temperature range 60 to 160 °C where ~90% of the intensity has disappeared at 130 °C. The ammine bimetallic borohydride $Li_2Mn(BH_4)_4 \cdot 6NH_3$ may decompose to $Mn(BH_4)_2 \cdot 6NH_3$, which immediately decomposes, and possibly also to amorphous $LiBH_4$.[49]

In situ SR-PXD data of s6 are shown in Figure 9a and S13, while Figure 9b shows integrated reflection intensities as
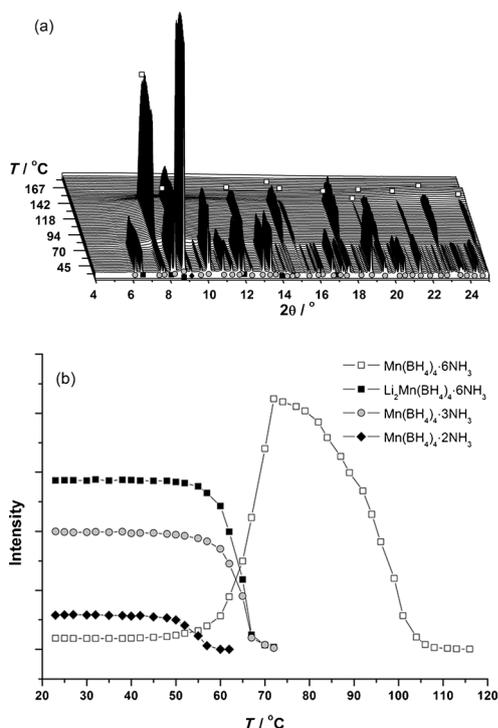
Figure 9. (a) In situ SR-PXD of $Mn(BH_4)_2 \cdot 6NH_3$-$Mn(BH_4)_2$ (3:3, s6) heated from RT to 200 °C (5 °C min^{-1}, $p(Ar) = 1$ bar, $\lambda = 0.823056$ Å). (b) Integration of selected reflections plotted as a function of the temperature. Symbols: ● $Mn(BH_4)_2 \cdot 3NH_3$; □ $Mn(BH_4)_2 \cdot 6NH_3$; ◆ $Mn(BH_4)_2 \cdot 2NH_3$; ■ $Li_2Mn(BH_4)_4 \cdot 6NH_3$.

a function of temperature. SR-PXD data at RT contain reflections from $Mn(BH_4)_2 \cdot 3NH_3$ (75.7 wt%), $Li_2Mn(BH_4)_4 \cdot 6NH_3$ (20.7 wt%), $Mn(BH_4)_2 \cdot 2NH_3$ (2.4 wt%), and $Mn(BH_4)_2 \cdot 6NH_3$ (1.3 wt%). Reflections for $Mn(BH_4)_2 \cdot 2NH_3$ disappear between 50 and 60 °C, while reflections from $Mn(BH_4)_2 \cdot 3NH_3$ and $Li_2Mn(BH_4)_4 \cdot 6NH_3$ decrease in intensity and disappear in the temperature range from 55 to 70 °C. When reflections from $Li_2Mn(BH_4)_4 \cdot 6NH_3$ and $Mn(BH_4)_2 \cdot 3NH_3$ disappear, reflections from $Mn(BH_4)_2 \cdot 6NH_3$ increase significantly in intensity (Figure 10b) and a broad hump in the background is observed. Upon further heating, reflections from $Mn(BH_4)_2 \cdot 6NH_3$ decrease in intensity at ~75 °C and disappear at 110 °C.

In situ SR-PXD collected for $Mn(BH_4)_2 \cdot 6NH_3$-$Mn(BH_4)_2$ (2:4, s7) is shown in Figure S16 (Supporting Information). At RT, weak reflections are observed for an unknown compound, **1** (~5 wt%) dominated by reflections from $Mn(BH_4)_2 \cdot 2NH_3$ (~95 wt%), which disappear at 45 and 77 °C, respectively, and no new reflections appear. In situ SR-PXD collected for $Mn(BH_4)_2 \cdot 6NH_3$-$Mn(BH_4)_2$ (1:5, s8) is shown in Figure S17 (Sup-
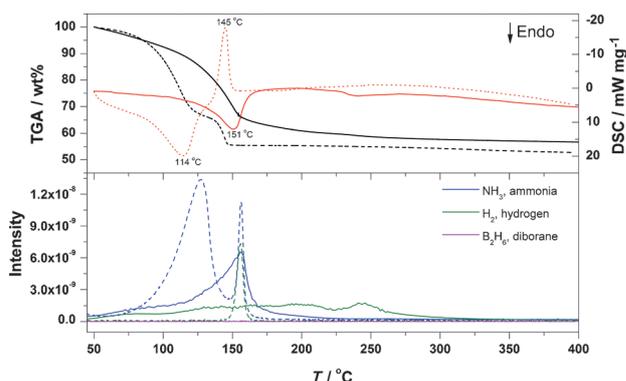
Figure 10. Thermogravimetric analysis and differential scanning calorimetry coupled with a mass spectrometer measured for $Mg(BH_4)_2 \cdot 6NH_3$ (s1, solid line) and $Mn(BH_4)_2 \cdot 6NH_3$ (s2, dashed line) heated from RT to 400 °C (5 °C min^{-1}). The upper diagram shows the TGA curves (black lines) and DSC-profiles (red lines), while the lower diagram shows the corresponding MS-signals.

porting Information). At RT, diffracted intensities from **2** and **3** are observed, which disappear at 52 and 41 °C, respectively, and no other Bragg peaks occur at higher temperatures. In situ SR-PXD data for $Mn(BH_4)_2 \cdot 6NH_3$-$LiBH_4$ (1:2, s9) (Supporting Information, Figure S18a) reveal reflections from **4** (~90 wt%) and $Li_2Mn(BH_4)_4 \cdot 6NH_3$ (~10 wt%) at RT. While reflections from **4** decrease in intensity and disappear at ~80 °C those from $Li_2Mn(BH_4)_4 \cdot 6NH_3$ increase in intensity with a maximum at ~77 °C and disappear at ~100 °C and no diffraction is observed at higher temperatures (Figure S18b). This may indicate that **4** is a less stable bimetallic ammine lithium manganese borohydride, for example, $Li_2Mn(BH_4)_4 \cdot 4NH_3$, that transforms into the more stable $Li_2Mn(BH_4)_4 \cdot 6NH_3$, and possibly $Mn(BH_4)_4$ and $LiBH_4$ upon heating.

For samples s4, s5, and s6 that contain both $Li_2Mn(BH_4)_4 \cdot 6NH_3$ and $Mn(BH_4)_2 \cdot 3NH_3$, reflections from both compounds disappear at ~60–65 °C and give rise to an increase in intensity for $Mn(BH_4)_2 \cdot 6NH_3$ in addition to an increased background. In contrast, in situ SR-PXD data for $Mn(BH_4)_2 \cdot 6NH_3$ and $Li_2Mn(BH_4)_4 \cdot 6NH_3$ (s2) and $Mn(BH_4)_2 \cdot 6NH_3$-$LiBH_4$ (1:2, s9) show that the reflections from $Li_2Mn(BH_4)_4 \cdot 6NH_3$ disappear at ~95 °C. This reflects that $Li_2Mn(BH_4)_4 \cdot 6NH_3$ and $Mn(BH_4)_2 \cdot 3NH_3$ react and may form a melt and solid $Mn(BH_4)_2 \cdot 6NH_3$ (see discussion above and Figure 9). In general, all the investigated samples decompose into amorphous products, which makes the detailed thermolysis mechanism challenging to investigate. Furthermore, the amorphous products cannot be analyzed by solid-state NMR due to the paramagnetic behavior of Mn^{2+}.

Thermal analysis and temperature-programmed photographic analysis

Thermogravimetric analysis, differential scanning calorimetry and simultaneous mass spectrometry (TGA/DSC-MS) have been measured for $Mg(BH_4)_2 \cdot 6NH_3$ (s1) and $Mn(BH_4)_2 \cdot 6NH_3$ and $Li_2Mn(BH_4)_4 \cdot 6NH_3$ (s2) in the temperature range from RT to 400 °C (5 °C min^{-1}), see Figure 10. The TGA data for

Mg(BH$_4$)$_2$·6NH$_3$ (s1) reveal a mass loss from RT to 175 °C of 37.1 wt%, which is slightly smaller than that of four molecules of NH$_3$ (theoretical 43.6 wt%). The MS signal (Figure 10, lower panel) reveals mainly NH$_3$ release at $T < 175$ °C, while mainly H$_2$ is released at $T > 175$ °C, which is in accord with the literature.[3,15,50] The DSC curve reveals an endothermic signal centered at 151 °C. In comparison MgCl$_2$·6NH$_3$ has an onset temperature for NH$_3$ release at ~80 °C and has released all NH$_3$ at 350 °C.[51]

In contrast, two distinct steps are observed for the thermal decomposition of s2 (Mn(BH$_4$)$_2$·6NH$_3$, 95.4 wt% and Li$_2$Mn(BH$_4$)$_4$·6NH$_3$, 4.6 wt%). First, a TGA mass loss of 32.8 wt% from RT to 125 °C associated with an endothermic DSC peak at 114 °C and a strong MS signal assigned to NH$_3$. Release of four NH$_3$ molecules from Mn(BH$_4$)$_2$·6NH$_3$ corresponds to a calculated mass loss of 36.5 wt%. A second mass loss of 11.7 wt% from 125 to 150 °C is observed, which is associated with sharp simultaneous MS signal (peak value at ~156 °C) of hydrogen and ammonia. The DSC data reveal a strong exothermic event with a maximum at $T = 145$ °C indicating a reaction between the protic H$^{\delta+}$ from NH$_3$ and the hydridic H$^{\delta-}$ from BH$_4^-$. Temperature-programmed photographic analysis (TPPA) shows that the white powder of s2 (Supporting Information, Figure S19) becomes darker during heating from RT to 138 °C and is black at 153 °C as a consequence of thermal decomposition. These results reveal that Mn(BH$_4$)$_2$·6NH$_3$ decomposes by thermolysis without melting and the volume of the sample remains approximately constant during the process.

TGA/DSC-MS has also been measured for Mn(BH$_4$)$_2$·6NH$_3$-Mn(BH$_4$)$_2$ (5:1, s4), (4:2, s5), (3:3, s6), (2:4, s7) and (1:5, s8) and Mn(BH$_4$)$_2$ heated from RT to 400 °C (5 °C min^{-1}). The TGA data (Figure 11) for neat Mn(BH$_4$)$_2$ ($\rho_m = 9.5$ wt% H$_2$) show a mass loss of 18.5 wt% in the temperature range from 125 to 175 °C, while the DSC data reveal an endothermic peak in the same temperature range. The MS signals (Figure 12) show that a mixture of diborane and hydrogen is released in accordance with the literature.[52,53] In addition, two weak endothermic events are observed by DSC at 106 and 272 °C corresponding to the phase transition and the melting of traces of LiBH$_4$ in the sample.

The TGA data for Mn(BH$_4$)$_2$·6NH$_3$-Mn(BH$_4$)$_2$ (1:5, s8) (10.9 wt% H$_2$) reveal a mass loss on 11 wt% between 60 and 150 °C, while the corresponding MS signals reveal a release of mainly H$_2$ and smaller amount of NH$_3$ with peaks with maxima at 129 and 131 °C, respectively. The 'anomalous' TGA curve is explained by TPPA data (Supporting Information, Figure S20) confirming partial melting at 45 °C. Foaming is observed to start at 54 °C possibly due to release of H$_2$ and NH$_3$, which further escalates at ~90 °C simultaneously with release of H$_2$ and NH$_3$. The sample volume increases approximately by a factor of ten after the heat treatment when the sample was cooled to RT, which is similar to the behavior of NH$_3$BH$_3$.[28]

The DSC data for Mn(BH$_4$)$_2$·6NH$_3$-Mn(BH$_4$)$_2$ (2:4, s7) (11.9 wt% H$_2$) reveal two endothermic peaks at 45 and 77 °C, Figure 11. These two events are caused by partly melting of a small amount of, 1, and Mn(BH$_4$)$_2$·2NH$_3$, respectively, as seen by TPPA (Supporting Information, Figure S21), which is also in agree-
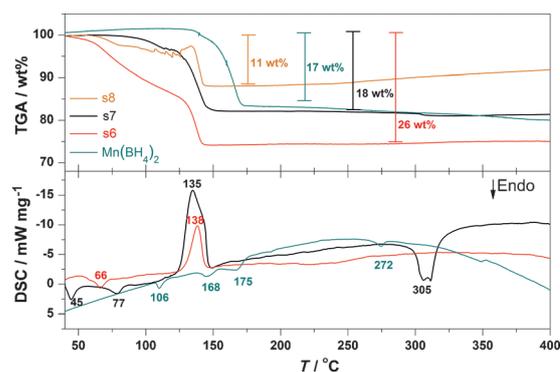

Figure 11. TGA/DSC for Mn(BH$_4$)$_2$ and Mn(BH$_4$)$_2$·6NH$_3$-Mn(BH$_4$)$_2$ (3:3, s6), (2:4, s7) and (1:5, s8) heated from RT to 400 °C (5 °C min^{-1}). DSC data for s8 are not shown.
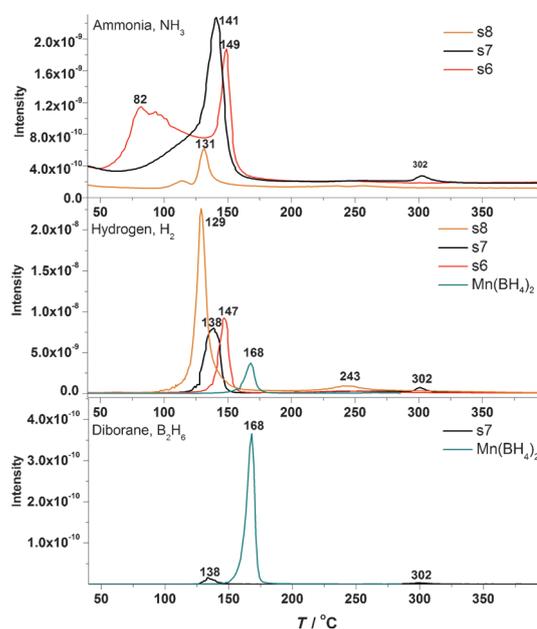
Figure 12. Mass spectrometer signals for NH$_3$ (upper), H$_2$ (middle) and B$_2$H$_6$ (lower) of Mn(BH$_4$)$_2$ and Mn(BH$_4$)$_2$·6NH$_3$-Mn(BH$_4$)$_2$ (3:3, s6), (2:4, s7) and (1:5, s8) heated from RT to 400 °C (5 °C min^{-1}).

ment with in situ SR-PXD (Figure S16). This is followed by a mass loss observed by TGA of 18 wt% from 77 to 160 °C with an exothermic peak with maximum at 135 °C. At elevated temperatures a mass loss of 0.6 wt% is observed, accompanied by an endothermic event with T_{min} at 305 °C. The MS data show that a mixture of H$_2$ and NH$_3$ are released below 160 °C. At ~300 °C, H$_2$ with traces of B$_2$H$_6$ are released, which may be caused by traces of LiBH$_4$ reacting with the decomposed Mn(BH$_4$)$_2$·2NH$_3$.

For Mn(BH$_4$)$_2$·6NH$_3$-Mn(BH$_4$)$_2$ (3:3, s6) (12.6 wt% H$_2$) a two-step decomposition is observed. First, a mass loss on 13 wt% of NH$_3$ is released in the range from 50 to 115 °C corresponding to one equivalent of NH$_3$ (theoretical 12.5 wt%). This is followed by a mass loss of 13 wt% in the range from 115 to 155 °C similar to s7. The MS signals reveal a release of a mixture of H$_2$ and NH$_3$ for the second reaction, and the DSC data
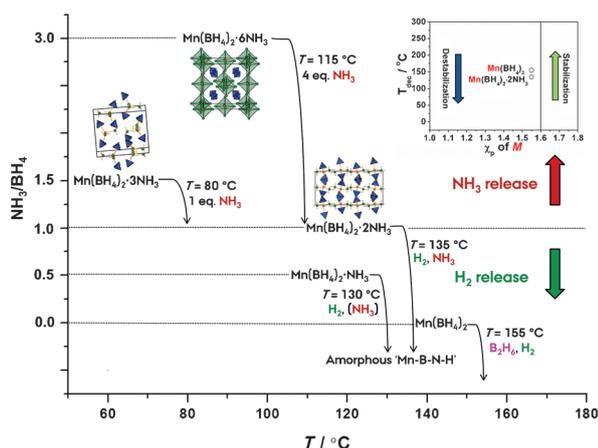
Figure 13. Illustration of decomposition temperatures and released gasses for ammine manganese borohydrides with varying NH_3/BH_4 ratios, that is, $Mn(BH_4)_2 \cdot nNH_3$ ($n = 1, 2, 3,$ and 6). NH_3 is released for $NH_3/BH_4 > 1.0$, while hydrogen is released for $NH_3/BH_4 \leq 1.0$. In contrast, $Mn(BH_4)_2$ releases B_2H_6 and H_2 upon decomposition. Metal borohydrides with low electronegativity ($1.6 < \chi_p$) are *destabilized* while those with high electronegativity ($1.6 > \chi_p$) are *stabilized* by formation of ammine metal borohydrides (see inset). $Mn(BH_4)_2 \cdot 2NH_3$ ($\chi_p(Mn) = 1.55$) is slightly destabilized by only ~20 °C compared to $Mn(BH_4)_2$.

reveal an exothermic event with maximum at 138 °C. At 66 °C, an endothermic event is observed, which is in accord with the disappearing of reflections from $Mn(BH_4)_2 \cdot 3NH_3$ and $Li_2Mn(BH_4)_4 \cdot 6NH_3$ observed by in situ SR-PXD (Figure 9 B). TPPA (Supporting Information, Figure S22) reveals that upon heating, at 73 °C, liquid droplets are seen on the surface of the glass vial confirming that the mixture partially melts. However, the produced $Mn(BH_4)_2 \cdot 6NH_3$ appears to float on top of the melt. In the temperature range from 137 to 159 °C the solid becomes darker due to the decomposition of $Mn(BH_4)_2 \cdot 6NH_3$ as seen on Figure S19. No thermal events are observed at $T > 155$ °C.

The PXD data reveal that $Mn(BH_4)_2 \cdot 6NH_3$-$Mn(BH_4)_2$ (4:2, s5) and $Mn(BH_4)_2 \cdot 6NH_3$-$Mn(BH_4)_2$ (5:1, s4) are physical mixtures of $Mn(BH_4)_2 \cdot 3NH_3$, $Mn(BH_4)_2 \cdot 6NH_3$ and $Li_2Mn(BH_4)_4 \cdot 6NH_3$. Therefore, the thermal decompositions are similar to those for $Mn(BH_4)_2 \cdot 3NH_3$ and $Mn(BH_4)_2 \cdot 6NH_3$, see Figures S23 and S24 (Supporting Information). TGA data reveal a three-step mass loss for s4 and s5 of 33 and 34 wt%, respectively, in the temperature range RT to 160 °C. The first mass loss occurs at 60 to 100 °C caused by decomposition of $Mn(BH_4)_2 \cdot 3NH_3$ and $Li_2Mn(BH_4)_4 \cdot 6NH_3$ releasing NH_3 and a small amount of H_2. The second step is caused by $Mn(BH_4)_2 \cdot 6NH_3$ initiated at ~80 °C releasing an additional amount NH_3. Thirdly, an exothermic reaction with a DSC peak maximum at 145 °C takes place releasing both H_2 and NH_3 similar to $Mn(BH_4)_2 \cdot 6NH_3$ (s2). Sample s5 has a minor mass loss of 0.5 wt% in the temperature range 290 and 305 °C, which is similar to $Mn(BH_4)_2 \cdot 6NH_3$-$Mn(BH_4)_2$ (2:4, s7).

In summary, both new compounds $Mn(BH_4)_2 \cdot 6NH_3$ and $Mn(BH_4)_2 \cdot 3NH_3$ initially release NH_3 followed by a release of a mixture of H_2 and minor amounts of NH_3 at higher temperatures, 135–140 °C similar to $Mn(BH_4)_2 \cdot 2NH_3$. However, the in situ

formation of $Mn(BH_4)_2 \cdot 2NH_3$ from $Mn(BH_4)_2 \cdot 6NH_3$ and $Mn(BH_4)_2 \cdot 3NH_3$ is not directly observed. This is similar to the magnesium-analogue, $Mg(BH_4)_2 \cdot 6NH_3$; a recent study reveals that the decomposition mechanism includes the intermediates $Mg(BH_4)_2 \cdot 3NH_3$ and $Mg(BH_4)_2 \cdot 2NH_3$, but observation of these compounds is strongly dependent on the heating rate.[15, 50]

$Mn(BH_4)_2 \cdot NH_3$ releases mainly H_2 with traces of NH_3 with maximum peaks ~130 °C similar to $Mg(BH_4)_2 \cdot NH_3$. H_2 evolution from $Mn(BH_4)_2 \cdot nNH_3$ ($n = 1, 2$) is likely caused by dihydrogen elimination, that is, a reaction between $H^{\delta+}$ and $H^{\delta-}$ in close proximity observed by a strong exothermic DSC signal. This reaction may explain the fact that diborane is not observed during decomposition of $Mn(BH_4)_2 \cdot NH_3$, in contrast to $Mn(BH_4)_2$ which releases a mixture of diborane and hydrogen.

Indeed, the physical behavior of the series of ammine manganese borohydrides varies upon thermal treatment. Whereas $Mn(BH_4)_2 \cdot 6NH_3$ slowly turns darker upon ammonia release, the mixture of $Mn(BH_4)_2 \cdot 3NH_3$ and $Li_2Mn(BH_4)_2 \cdot 6NH_3$ melts at 66 °C. This is similar to the physical behavior of monometallic borohydrides and borohydride eutectic mixtures recently investigated.[34]

Ex situ investigations of preheated samples

Fractions of s7, $Mn(BH_4)_2 \cdot 2NH_3$ (~95 wt%) and **1** (~5 wt%), and s8, **2** (~25 wt%) and **3** (~75 wt%), were heated to 150 °C for 1 h in argon atmosphere and subsequently cooled to RT (denoted s7_150 and s8_150) and characterized by FTIR and PXD. The PXD data (Supporting Information, Figure S25) reveal the presence of only amorphous compounds. The FTIR data for s8 and s8_150 are compared in Figure S26 (Supporting Information), which clearly shows that all N-H and B-H absorption bands disappear after heating to 150 °C. s8_150 only reveals broad signals between 1500 and 500 cm^{-1}, which may be assigned to B—N bonds in accord with previous investigations of ammine metal borohydrides.[23, 44]

Hydrogen uptake has also been examined for s7_150 at $T = 250$ °C, $p(H_2) = 145$ bar for 16 h. However, no changes in the measured FTIR or PXD data for the sample before and after this treatment were observed (Figure S25 and S26), reflecting that hydrogen uptake did not occur at these conditions.

Ammine magnesium-manganese borohydride solid solutions

Inspired by the structural similarities between $Mg(BH_4)_2$, $Mn(BH_4)_2$, and $Mg_{1-x}Mn_x(BH_4)_2$ ($x \approx 0.10$),[54] an ammine metal borohydride solid solution of metal cations has been examined. Similar to the procedure used earlier, a mixture of α-$Mg(BH_4)_2$ and $Mn(BH_4)_2$ has been ball-milled (s10) and subsequently characterized by SR-PXD (Supporting Information, Figure S27). The extracted unit cell parameters from Rietveld refinement of SR-PXD data measured at identical physical conditions are compared with unit cell parameters for neat α-$Mg(BH_4)_2$ and $Mn(BH_4)_2$, see Table 4. The unit cell volume per formula unit (V/Z) has increased by 1.95% after ball milling with $Mn(BH_4)_2$, which suggests formation of a solid solution,

Table 4. Unit cell parameters extracted from Rietveld refinement of SR-PXD data collected at identical physical conditions.

Sample	Compound	a [Å]	c [Å]	V/Z [Å^3]	$\Delta(V/Z)$ [%]
–	$Mn(BH_4)_2$	10.43264(3)	10.90227(4)	114.18(1)	–
–	$Mg(BH_4)_2$	10.36413(7)	37.16383(4)	115.24(1)	0.93[a]
s10	$Mn(BH_4)_2$	10.4463(7)	10.906(2)	114.52(2)	0.30[a]
s10	$Mg_{1-x}Mn_x(BH_4)_2$	10.416(2)	37.168(9)	116.41(3)	1.95[a]
s1	$Mg(BH_4)_2 \cdot 6NH_3$	10.7948(2)		314.47(1)	–
s2	$Mn(BH_4)_2 \cdot 6NH_3$	10.83410(2)		317.92(1)	1.10[b]
s11	$Mg_{0.5}Mn_{0.5}(BH_4)_2 \cdot 6NH_3$	10.82466(9)		317.09(1)	0.83[b]

[a] Compared to V/Z for $Mn(BH_4)_2$. [b] Compared to V/Z for $Mg(BH_4)_2 \cdot 6NH_3$.

$Mg_{1-x}Mn_x(BH_4)_2$ in accord with a previous study.[54] The sample s10 has been reacted with NH_3 (s11) and characterized by SR-PXD (Supporting Information, Figure S28). Again, the unit cell volume per formula unit (V/Z) for s11 is compared with parameters for $Mg(BH_4)_2 \cdot 6NH_3$ (s1) and $Mn(BH_4)_2 \cdot 6NH_3$ (s2). This suggests formation of a solid solution $Mg_{0.5}Mn_{0.5}(BH_4)_2 \cdot 6NH_3$ with (V/Z) in between the values for $Mg(BH_4)_2 \cdot 6NH_3$ and $Mn(BH_4)_2 \cdot 6NH_3$.

The thermal decomposition of $Mg_{0.5}Mn_{0.5}(BH_4)_2 \cdot 6NH_3$ (s11) has been investigated by TGA/DSC-MS (Figure S27–S28) and reveals only slightly modification of the decomposition properties compared to the pristine samples. The DSC signals (Supporting Information, Figure S29) reveal that the temperatures for the exothermic peak are at 140 and 145 °C for $Mg_{0.5}Mn_{0.5}(BH_4)_2 \cdot 6NH_3$ (s11) and $Mn(BH_4)_2 \cdot 6NH_3$ (s2), respectively. Furthermore, the MS signals (Supporting Information, Figure S30) reveal that the temperatures for maximum NH_3 release are at 146 and 156 °C for s11 and s2, respectively.

Trends for ammine metal borohydrides

Ammonia is harmful for low-temperature fuel cells and the gas release from energy storage materials needs to be tailored by materials design to avoid NH_3 release. Here, we demonstrated that the ratio between the amount of ammonia and borohydride, denoted n/m-ratio in $M(BH_4)_m \cdot nNH_3$, can be adjusted by mechanochemical treatment of $M(BH_4)_m \cdot nNH_3$-$M(BH_4)_m$ mixtures in various ratios. $Mn(BH_4)_2 \cdot 6NH_3$ and $Mn(BH_4)_2 \cdot 3NH_3$ release ammonia, while $Mn(BH_4)_2 \cdot 2NH_3$ and $Mn(BH_4)_2 \cdot NH_3$ release increasing amounts of hydrogen and limited amounts of ammonia (Figure 13). This suggests that the number of ammonia molecules in the solid should preferably be equal to or lower than the amount of borohydride complexes to avoid release of ammonia, that is, $n/m \leq 1$.

This is also observed for the series of ammine magnesium borohydride.[15,26] On the other hand, hydrogen (95 % purity) is released for $Al(BH_4)_3 \cdot 6NH_3$ with $n/m = 2$.[19] This may be explained by the different strength of the dihydrogen bonds between protic and hydridic hydrogens. Both $Al(BH_4)_3 \cdot 6NH_3$ and $Mg(BH_4)_2 \cdot 6NH_3$ consist of $[M(NH_3)_6]^{m+}$ complex cations surrounded by BH_4^- anions.[18] However, the dihydrogen bonds, $H^{\delta+} \cdots H^{\delta-}$, in $Al(BH_4)_3 \cdot 6NH_3$ are relatively short and strong, between 1.91–2.19 Å, while above 2.12 Å for $Mg(BH_4)_2 \cdot 6NH_3$. Mn^{2+} coordinates to three ammonia ligands and two borohy-

dride groups in $Mn(BH_4)_2 \cdot 3NH_3$. Despite the short distance between NH_3 and BH_4^-, NH_3 is still released. In contrast, Mn^{2+} in $Mn(BH_4)_2 \cdot 2NH_3$ is coordinated to two BH_4^- and two NH_3 groups giving rise to hydrogen release. In summary, the coordination of Mn^{2+} to nitrogen in ammonia is decreasing and with increasing coordination to BH_4^- which decreases the ammonia gas released.

For the ammine compounds based on the more stable metal borohydrides such as $LiBH_4$ or $Ca(BH_4)_2$, ammonia is released at ~120 and 140 °C, respectively, from open systems, that is, $p(NH_3) \sim 0$, even though the n/m ratio is 'optimal' (i.e., $n/m \leq 1$) and the crystal structures contain strong dihydrogen bonds.[20,55] On the other hand, hydrogen is released in closed systems, $p(NH_3) > 0$, during thermolysis of $Li(NH_3)_{4/3}BH_4$ and $Ca(BH_4)_2 \cdot 2NH_3$, which in fact suggests that hydrogen is released in a solid-gas dihydrogen elimination reaction between the metal borohydride and ammonia gas. Metal borohydrides with low electronegativity of the metals are destabilized by ammonia, while metal borohydrides with high electronegativity of the metals are stabilized by ammonia.[3] Ammine metal borohydrides with electronegativity of the metal in the range $1.35 < \chi_p < 1.6$ have so far not been reported. Hence, the limit for destabilization and stabilization remain unknown. We show that $Mn(BH_4)_2$ ($\chi_p(Mn) = 1.55$) is slightly destabilized by only ~20 °C by formation of $Mn(BH_4)_2 \cdot 2NH_3$, revealing that the limit is in the range $\chi_p \approx 1.55$ to 1.61 (Figure 13 inset), since $Al(BH_4)_3$ ($\chi_p(Al) = 1.61$) is stabilized by formation of $Al(BH_4)_3 \cdot 6NH_3$.[19] The destabilization is likely caused by dihydrogen elimination from protic hydrogen, $H^{\delta+}$ in NH_3 and hydridic hydrogen, $H^{\delta-}$ from BH_4^-. On the other hand, the stabilization may be due to shielding of metals with high electronegativity ($\chi_p > 1.6$) by complex formation. As mentioned earlier, $Zn(BH_4)_2 \cdot 2NH_3$ releases 8.9 wt % H_2 at $T < 115$ °C within 15 min in contrast to $LiZn_2(BH_4)_5$ which releases a mixture of diborane and hydrogen via reduction of Zn^{2+} to Zn.[13,21,56] Furthermore, $Mn(BH_4)_2 \cdot 2NH_3$, in contrast to $Mn(BH_4)_2$, does not release diborane, which is likely a consequence of the strong intermolecular dihydrogen interactions. These results may open new possibility for rational materials design and tailoring materials properties towards reversible hydrogen storage. However a major challenge for ammine metal borohydrides is the formation of stable decomposition products with strong B–N bonds that hamper hydrogen uptake. Future research may also address this issue, for example, by detailed analysis of the reaction mechanism for hydrogen absorption of dehydrogenated nanoconfined $Al(BH_4)_3 \cdot 6NH_3$ treated with hydrazine in liquid ammonia similar to other B-N based materials.[24,57–61]

Conclusions

A new series of halide- and solvent-free ammine manganese borohydrides have been synthesized combining solvent-based methods and mechanochemistry. Four crystal structures have been successfully solved using synchrotron powder X-ray diffraction data: $Mn(BH_4)_2 \cdot 2NH_3$, $Mn(BH_4)_2 \cdot 3NH_3$, $Mn(BH_4)_2 \cdot 6NH_3$,

and $Li_2Mn(BH_4)_4\cdot6NH_3$, and the first ammine metal borohydride solid solution is presented, $Mn_{0.5}Mg_{0.5}(BH_4)_2\cdot6NH_3$. Furthermore, structures of ammine magnesium borohydrides are revisited and new structural models for $Mg(BH_4)_2\cdot3NH_3$ and $Li_2Mg(BH_4)_4\cdot6NH_3$ are presented, which are isostructural to the manganese analogues presented in this study. Thermal decomposition has been systematically investigated for all samples by in situ SR-PXD, temperature-programmed photographic analysis and simultaneous thermogravimetric analysis, differential scanning calorimetry and mass spectrometry. Upon thermal treatment $Mn(BH_4)_2\cdot6NH_3$ and $Mn(BH_4)_2\cdot3NH_3$ release first NH_3 followed by a release of a mixture of H_2 and NH_3 similar to $Mn(BH_4)_2\cdot2NH_3$. On the other hand, increased H_2 purity and lower temperature for decomposition is obtained for $Mn(BH_4)_2\cdot NH_3$. In contrast to $Mn(BH_4)_2$, none of the $Mn(BH_4)_2\cdot nNH_3$ compounds release diborane. This may be a consequence of the dihydrogen elimination from dihydrogen bonds between partly negative and partly positive hydrogen atoms of NH_3 and BH_4, respectively. We show that the n/m ratio for $M(BH_4)_m\cdot nNH_3$ may be modified by mechanochemical treatment of $M(BH_4)_m\cdot nNH_3$-$M(BH_4)_m$ mixtures in various ratios and thereby the hydrogen purity is increased for the released gas. Finally, it has been evaluated that destabilization is observed for metal borohydrides with low electronegativity ($\chi_p < 1.6$), while metal borohydrides with high electronegativity ($\chi_p > 1.6$) are stabilized by formation of new ammonia containing compounds. This relationship may lead to the rational design of novel compounds with desired properties for energy storage.

Acknowledgements

Keywords: hydrogen storage · hydrides · synchrotron radiation · x-ray diffraction · mechanochemistry

[1] S. I. Orimo, Y. Nakamori, J. R. Eliseo, A. Züttel, C. M. Jensen, *Chem. Rev.* **2007**, *107*, 4111 – 4132.

[2] L. Schlapbach, A. Züttel, *Nature* **2001**, *414*, 353 – 358.

[3] L. H. Jepsen, M. B. Ley, Y.-S. Lee, Y. W. Cho, M. Dornheim, J. O. Jensen, Y. Filinchuk, J. E. Jørgensen, F. Besenbacher, T. R. Jensen, *Mater. Today* **2014**, *17*, 129 – 135.

[4] M. B. Ley, L. H. Jepsen, Y.-S. Lee, Y. W. Cho, J. M. Bellosta von Colbe, M. Dornheim, M. Rokni, J. O. Jensen, M. Sloth, Y. Filinchuk, et al., *Mater. Today* **2014**, *17*, 122 – 128.

[5] L. H. Rude, T. K. Nielsen, D. B. Ravnsbæk, U. Bösenberg, M. B. Ley, B. Richter, L. M. Arnbjerg, M. Dornheim, Y. Filinchuk, F. Besenbacher, et al., *Phys. Status Solidi* **2011**, *208*, 1754 – 1773.

[6] W. I. F. David, *Faraday Discuss.* **2011**, *151*, 399.

[7] J. Huot, D. B. Ravnsbæk, J. Zhang, F. Cuevas, M. Latroche, T. R. Jensen, *Prog. Mater. Sci.* **2013**, *58*, 30 – 75.

[8] P. Schouwink, M. B. Ley, A. Tissot, H. Hagemann, T. R. Jensen, Ľ. Smrčok, R. Černý, *Nat. Commun.* **2014**, *5*, 5706.

[9] H. W. Li, S. I. Orimo, Y. Nakamori, K. Miwa, N. Ohba, S. Towata, A. Züttel, *J. Alloys Compd.* **2007**, *446*, 315 – 318.

[10] A. Züttel, A. Borgschulte, S. I. Orimo, *Scr. Mater.* **2007**, *56*, 823 – 828.

[11] Y. Nakamori, K. Miwa, A. Ninomiya, H. Li, N. Ohba, S. Towata, A. Züttel, S. I. Orimo, *Phys. Rev. B* **2006**, *74*, 45126.

[12] G. N. Schrauzer, *Naturwissenschaften* **1955**, *42*, 438 – 438.

[13] D. Ravnsbæk, Y. Filinchuk, Y. Cerenius, H. J. Jakobsen, F. Besenbacher, J. Skibsted, T. R. Jensen, *Angew. Chem. Int. Ed.* **2009**, *48*, 6659 – 6663; *Angew. Chem.* **2009**, *121*, 6787 – 6791.

[14] D. B. Ravnsbæk, L. H. Sørensen, Y. Filinchuk, F. Besenbacher, T. R. Jensen, *Angew. Chem. Int. Ed.* **2012**, *51*, 3582 – 3586; *Angew. Chem.* **2012**, *124*, 3642 – 3646.

[15] G. Soloveichik, J.-H. Her, P. W. Stephens, Y. Gao, J. Rijssenbeek, M. Andrus, J.-C. Zhao, *Inorg. Chem.* **2008**, *47*, 4290 – 4298.

[16] X. Zheng, G. Wu, W. Li, Z. Xiong, T. He, J. Guo, H. Chen, P. Chen, *Energy Environ. Sci.* **2011**, *4*, 3593.

[17] Y. Guo, H. Wu, W. Zhou, X. Yu, *J. Am. Chem. Soc.* **2011**, *133*, 4690 – 4693.

[18] Z. Tang, Y. Tan, H. Wu, Q. Gu, W. Zhou, C. M. Jensen, X. Yu, *Acta Mater.* **2013**, *61*, 4787 – 4796.

[19] Y. Guo, X. Yu, W. Sun, D. Sun, W. Yang, *Angew. Chem. Int. Ed.* **2011**, *50*, 1087 – 1091; *Angew. Chem.* **2011**, *123*, 1119 – 1123.

[20] Z. Tang, Y. Tan, Q. Gu, X. Yu, *J. Mater. Chem.* **2012**, *22*, 5312 – 5318.

[21] Q. Gu, L. Gao, Y. Guo, Y. Tan, Z. Tang, K. S. Wallwork, F. Zhang, X. Yu, *Energy Environ. Sci.* **2012**, *5*, 7590 – 7600.

[22] R. Černý, D. B. Ravnsbæk, P. Schouwink, Y. Filinchuk, N. Penin, J. Teyssier, L. Smrčok, T. R. Jensen, *J. Phys. Chem. C* **2012**, *116*, 1563 – 1571.

[23] F. Yuan, Q. Gu, Y. Guo, W. Sun, X. Chen, X. Yu, *J. Mater. Chem.* **2012**, *22*, 1061 – 1068.

[24] Z. Tang, F. Yuan, Q. Gu, Y. Tan, X. Chen, C. M. Jensen, X. Yu, *Acta Mater.* **2013**, *61*, 3110 – 3119.

[25] M. Li, F. Yuan, Q. Gu, X. Yu, *Int. J. Hydrogen Energy* **2013**, *38*, 9236 – 9242.

[26] Y. Yang, Y. Liu, Y. Li, M. Gao, H. Pan, *Chem. Asian J.* **2013**, *8*, 476 – 481.

[27] Y. Filinchuk, B. Richter, T. R. Jensen, V. Dmitriev, D. Chernyshov, H. Hagemann, *Angew. Chem. Int. Ed.* **2011**, *50*, 11162 – 11166; *Angew. Chem.* **2011**, *123*, 11358 – 11362.

[28] L. H. Jepsen, V. Ban, K. T. Møller, Y.-S. Lee, Y. W. Cho, F. Besenbacher, Y. Filinchuk, J. Skibsted, T. R. Jensen, *J. Phys. Chem. C* **2014**, *118*, 12141 – 12153.

[29] T. R. Jensen, T. K. Nielsen, Y. Filinchuk, J.-E. Jørgensen, Y. Cerenius, E. M. Gray, C. J. Webb, *J. Appl. Crystallogr.* **2010**, *43*, 1456 – 1463.

[30] A. P. Hammersley, S. O. Svensson, M. Hanfland, A. N. Fitch, D. Hausermann, *High Press. Res.* **1996**, *14*, 235 – 248.

[31] A. Boultif, D. Louër, *J. Appl. Crystallogr.* **2004**, *37*, 724 – 731.

[32] V. Favre-Nicolin, R. Cerný, *J. Appl. Crystallogr.* **2002**, *35*, 734 – 743.

[33] A. L. Spek, *Acta Crystallogr. Sect. D* **2009**, *65*, 148 – 155.

[34] M. Paskevicius, M. B. Ley, D. A. Sheppard, T. R. Jensen, C. E. Buckley, *Phys. Chem. Chem. Phys.* **2013**, *15*, 19774 – 19789.

[35] N. A. Tumanov, D. A. Safin, B. Richter, Z. Łodziana, T. R. Jensen, Y. Garcia, Y. Filinchuk, *Dalton Trans.* **2015**, DOI: 10.1039/C4DT03807J.

[36] H. Reardon, J. M. Hanlon, M. Grant, I. Fullbrook, D. H. Gregory, *Crystals* **2012**, *2*, 193 – 212.

[37] R. D. Shannon, *Acta Crystallogr. Sect. A* **1976**, *32*, 751 – 767.

[38] W. Sun, X. Chen, Q. Gu, K. S. Wallwork, Y. Tan, Z. Tang, X. Yu, *Chem. Eur. J.* **2012**, *18*, 6825 – 6834.

[39] L. H. Rude, M. Corno, P. Ugliengo, M. Baricco, Y.-S. Lee, Y. W. Cho, F. Besenbacher, J. Overgaard, T. R. Jensen, *J. Phys. Chem. C* **2012**, *116*, 20239 – 20245.

[40] F. C. Gennari, L. Fernández Albanesi, I. J. Rios, *Inorg. Chim. Acta* **2009**, *362*, 3731 – 3737.

[41] S. Aldridge, A. J. Blake, A. J. Downs, R. O. Gould, S. Parsons, C. R. Pulham, *J. Chem. Soc. Dalton Trans.* **1997**, 1007 – 1012.

[42] Y. Filinchuk, H. Hagemann, *Eur. J. Inorg. Chem.* **2008**, 3127 – 3133.

[43] Y. Filinchuk, D. Chernyshov, R. Černý, *J. Phys. Chem. C* **2008**, *112*, 10579 – 10584.

[44] G. Xia, Q. Gu, Y. Guo, X. Yu, *J. Mater. Chem.* **2012**, *22*, 7300 – 7307.

[45] Y. Yang, Y. Liu, H. Wu, W. Zhou, M. Gao, H. Pan, *Phys. Chem. Chem. Phys.* **2014**, *16*, 135–143.

[46] I. Olovsson, D. H. Templeton, *Acta Crystallogr.* **1959**, *12*, 832–836.

[47] J. P. Soulié, G. Renaudin, R. Cerny, K. Yvon, *J. Alloys Compd.* **2002**, *346*, 200–205.

[48] V. D'Anna, A. Spyratou, M. Sharma, H. Hagemann, *Spectrochim. Acta Part A* **2014**, *128*, 902–906.

[49] D. B. Ravnsbæk, Y. Filinchuk, R. Cerny, M. B. Ley, D. Haase, H. J. Jakobsen, J. Skibsted, T. R. Jensen, *Inorg. Chem.* **2010**, *49*, 3801–3809.

[50] Y. Yang, Y. Liu, Y. Li, M. Gao, H. Pan, *J. Phys. Chem. C* **2013**, *117*, 16326–16335.

[51] C. H. Christensen, R. Z. Sørensen, T. Johannessen, U. J. Quaade, K. Honkala, T. D. Elmøe, R. Køhler, J. K. Nørskov, *J. Mater. Chem.* **2005**, *15*, 4106–4108.

[52] R. Liu, D. Reed, D. Book, *J. Alloys Compd.* **2012**, *515*, 32–38.

[53] R. A. Varin, L. Zbroniec, M. Polanski, Y. Filinchuk, R. Černý, *Int. J. Hydrogen Energy* **2012**, *37*, 16056–16069.

[54] R. Černý, N. Penin, V. d'Anna, J. Ruziska, *Acta Mater.* **2011**, *59*, 5171–5180.

[55] S. R. Johnson, W. I. F. David, D. M. Royse, M. Sommariva, C. Y. Tang, F. P. A. Fabbiani, M. O. Jones, P. P. Edwards, *Chem. Asian J.* **2009**, *4*, 849–854.

[56] O. Friedrichs, A. Remhof, S. Hwang, A. Züttel, *Chem. Mater.* **2010**, *22*, 3265–3268.

[57] Z. Tang, Y. Tan, X. Chen, L. Ouyang, M. Zhu, D. Sun, X. Yu, *Angew. Chem. Int. Ed.* **2013**, *52*, 12659–12663; *Angew. Chem.* **2013**, *125*, 12891–12895.

[58] A. D. Sutton, A. K. Burrell, D. A. Dixon, E. B. Garner, J. C. Gordon, T. Nakagawa, K. C. Ott, J. P. Robinson, M. Vasiliu, *Science* **2011**, *331*, 1426–1429.

[59] Z. Tang, H. Chen, X. Chen, L. Wu, X. Yu, *J. Am. Chem. Soc.* **2012**, *134*, 5464–5467.

[60] Z. Tang, X. Chen, H. Chen, L. Wu, X. Yu, *Angew. Chem. Int. Ed.* **2013**, *52*, 5832–5835; *Angew. Chem.* **2013**, *125*, 5944–5947.

[61] F. Yuan, Q. Gu, X. Chen, Y. Tan, Y. Guo, X. Yu, *Chem. Mater.* **2012**, *24*, 3370–3379.